Applied Physics Letters

Far-infrared surface-plasmon quantum-cascade lasers at 21.5 μm and 24 μm wavelengths

Cite as: Appl. Phys. Lett. **78**, 2620 (2001); https://doi.org/10.1063/1.1367304
Submitted: 15 February 2001 . Accepted: 05 March 2001 . Published Online: 25 April 2001

Raffaele Colombelli, Federico Capasso, Claire Gmachl, Albert L. Hutchinson, Deborah L. Sivco, Alessandro Tredicucci, Michael C. Wanke, A. Michael Sergent, and Alfred Y. Cho

Far-infrared surface-plasmon quantum-cascade lasers at 21.5 μm and 24 μm wavelengths

Raffaele Colombelli,[a] Federico Capasso, Claire Gmachl, Albert L. Hutchinson, Deborah L. Sivco, Alessandro Tredicucci,[b] Michael C. Wanke, A. Michael Sergent, and Alfred Y. Cho
Bell Laboratories, Lucent Technologies, 600 Mountain Avenue, Murray Hill, New Jersey 07974

(Received 15 February 2001; accepted for publication 5 March 2001)

Quantum-cascade lasers operating above 20 μm (at $\lambda\sim21.5$ μm and $\lambda\sim24$ μm) wavelength are reported. Pulsed operation was obtained up to 140 K and with a peak power of a few milliwatts at cryogenic temperatures. Laser action originates from interminiband transitions in ''chirped'' superlattice active regions. The waveguides are based on surface-plasmon modes confined at a metal–semiconductor interface. The wavelengths were chosen in order to avoid major phonon absorption bands, which are particularly strong at energies just above the reststrahlen band. We also report on a 21.5-μm-wavelength laser based on a two-sided interface-plasmon waveguide. © *2001 American Institute of Physics.* [DOI: 10.1063/1.1367304]

Quantum-cascade (QC) lasers have rapidly established themselves as tunable coherent sources in the midinfrared range of the electromagnetic spectrum.[1] Research has since expanded to other material systems, ultra-high-speed operation, and mode locking,[2,3] and the exploration of different frequency ranges.[4–6] The extension to the far-infrared range is of particular interest due to the lack of narrow-band, powerful, and compact sources in this wavelength range, but presents a formidable challenge related to physics issues and technical difficulties. Increased accuracy in the band-structure design becomes one of the key factors to assure high-electron-injection efficiency and to prevent hot-carrier effects. At these very long wavelengths, in proximity of the reststrahlen band,[7] anomalies in the dielectric constant of the semiconductor complicate laser operation; free-carrier absorption (increasing approximately with λ^2, λ being the wavelength) becomes the dominant factor for the optical losses, and electron–electron scattering can no longer be ignored as a nonradiative relaxation channel. Various types of waveguide concepts have to be adopted[8] in order to reduce the otherwise prohibitive layer thickness, enhance the optical confinement, and control the waveguide loss.

The waveguide design of choice for long wavelengths ($\lambda>15$ μm) is a metal–semiconductor waveguide based on surface plasmons.[8] The latter are transverse magnetic (TM) electromagnetic modes propagating at the interface between materials with dielectric constants of opposite signs. Since negative dielectric constants are typical of metals below the plasma frequency, the metal–semiconductor interface is an excellent waveguiding solution for long-wavelength QC lasers, given also the TM polarization of the intersubband emission. The waveguides are particularly attractive for long wavelengths where the reduced penetration of the mode into the metal leads to reduced waveguide losses and, at the same time, higher confinement factors Γ with respect to a dielectric waveguide. This is essential to reduce the otherwise prohibitively high laser-threshold current density at $\lambda>20$ μm. Surface-plasmon waveguides also limit the thickness of the epitaxially grown semiconductor material to a few micrometers.

In this letter, we report the realization of surface-plasmon QC lasers operating above 20 μm wavelength, i.e., in the far-infrared range of the electromagnetic spectrum, in particular, at $\lambda\sim21.5$ μm (sample D2691) and $\lambda\sim24$ μm (sample D2696), i.e., with 57.7 and 51.7 meV optical transition energy, respectively. Laser action is achieved up to maximum temperatures of 140 and 130 K, respectively, with a maximum output power of a few mW. These are the longest wavelength III–V semiconductor lasers to date: their emission frequencies lie at the edge of the reststrahlen region for the InGaAs/AlInAs system (approximately, from 30 to 50 μm wavelengths). The specific choice of the design wavelengths was, in fact, guided by the presence of minima in the $In_{0.53}Ga_{0.47}As$ and InP two-phonon absorption spectrum (the latter is the material of the lower cladding layer of the waveguide).[7] The absorption spectrum of any III–V semiconductor at frequencies just above the reststrahlen band consists of many intense absorption features related to two-phonon processes.[7] As these processes add optical loss to free-carrier absorption, it is important to avoid them to reduce the laser threshold.

Both laser structures have been grown by molecular-beam epitaxy using an $In_{0.53}Ga_{0.47}As/Al_{0.48}In_{0.52}As$ lattice matched to a low-doped ($n\sim2\times10^{17}$ cm^{-3}) InP substrate. The active regions of both lasers are based on interminiband transitions in ''chirped'' undoped superlattices[9] (see Fig. 1). The choice of this type of active region design is motivated by the low-doping requirement for the injectors, which is very advantageous at long wavelengths in order to reduce free-carrier absorption. Laser action takes place across the minigap between the second (II) and first (I) minibands, where large optical dipole matrix elements of $z=4.6$ nm and $z=4.8$ nm, respectively,[10] are computed. Extreme care has been taken in order to keep the energy separation between the individual states of miniband II close to the longitudinal optical (LO) phonon energy ($E_{LO}\sim34$ meV). This facilitates

[a]Electronic mail: colombel@physics.bell-labs.com
[b]Present address: Scuola Normale Superiore and INFM, Piazza dei Cavalieri 7, 56126 Pisa, Italy.

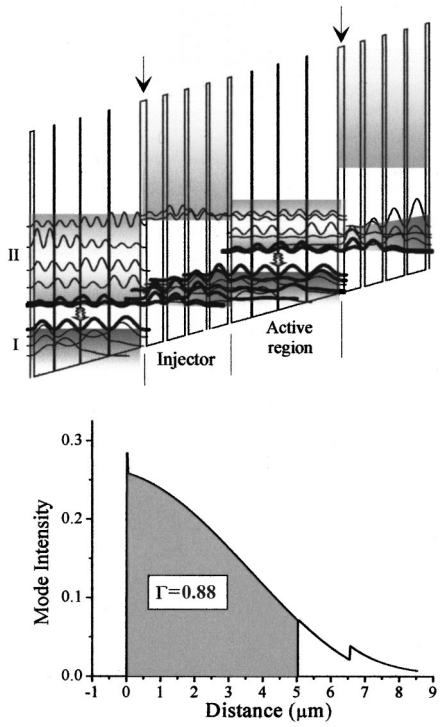

FIG. 1. Upper figure: Conduction-band profile of two periods (active region +injector) of sample D2696 ($\lambda=24$ μm) under an applied electric field of 15 kV/cm. The layer thicknesses in nanometers of a single stage are, from left to right starting from the injection barrier (indicated by an arrow): **1.45**/7.7/**0.4**/9.7/**0.35**/10.7/**0.45**/11.9/**2.4**/6.4/**1.6**/6.8/**1.4**/7.0/**1.2**/7.0. AlInAs layers are in bold. The moduli squared of the wave functions of each state of the miniband are shown; wavy arrows indicate the lasing transition. Sample D2691—which is not shown—has a similar layer structure with layer thicknesses: **1.5**/7.4/**0.45**/9.3/**0.4**/10.2/**0.5**/11.2/**2.65**/5.85/**1.6**/6.2/**1.4**/6.4/**1.2**/6.5. The underlined layers are doped to $n=2\times10^{17}$ cm^{-3}. The operating electric field is 17 kV/cm. Lower figure: Intensity profile of the surface-plasmon mode for the $\lambda=24$ μm laser.

fast electron relaxation.[11] Very narrow barriers, few Å thick, are necessary to achieve this task, thus posing stringent requirements on the growth quality. The ratios between the calculated lifetimes of the lower laser level (at the top of miniband I) ($\tau_1=0.6$ and 0.7 ps, for $\lambda=21.5$ μm and $\lambda=24$ μm, respectively), and the nonradiative scattering time between the laser levels ($\tau_{21}=2.6$ and 2.4 ps, respectively), ensure population inversion.[12] The active regions are bridged by specially designed injectors which extract electrons from miniband I of one superlattice active region and inject them into miniband II of the following one.

Forty and 65 active region/injector stages, were grown for the $\lambda=21.5$ and 24 μm laser; the growth of this cascade stack was preceded by a 1500-nm-thick InGaAs layer doped to $n\sim7\times10^{16}$ cm^{-3} and was followed by contact-facilitating layers (40 nm of $n\sim1\times10^{17}$ cm^{-3} doped InGaAs and 10 nm of highly doped n^{++} InGaAs). The wafers were processed into ridges of various widths (31–46 μm) by optical contact lithography and wet-chemical etching; after deposition of SiO_2 on the sides for insulation, top and back contacts (see Ref. 13) were deposited, leaving a wide portion of the top of the stripes open for deposition of a moderately thick (300 nm) surface-plasmon-carrying gold layer.[8] The intensity profile of the surface-plasmon mode (shown in Fig. 1 for sample D2696), was calculated via a transfer-matrix technique; dielectric constants for the doped

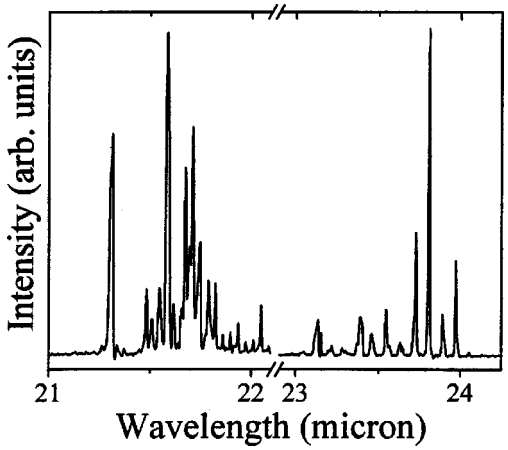

FIG. 2. Pulsed (50 ns pulse width, 84 kHz repetition rate) emission spectra of sample D2691 (left) and sample D2696 (right). Devices are 36 μm wide and 750 μm long. The drive currents were 1.6 and 1.75 A, respectively. The spectra were measured in rapid scan using a Nicolet Fourier transform infrared spectrometer and a He-cooled Si bolometer. The spectral resolution was set to 0.125 cm^{-1}.

semiconductor layers were calculated using a Drude–Lorentz model. A high-confinement factor of $\Gamma=0.76$, a waveguide loss of $\alpha_w=42$ cm^{-1}, and an effective refractive index of $n_{\text{eff}}=3.3$ are calculated for sample D2691. The values for sample D2696 are instead $\Gamma=0.88$, $\alpha_w=41$ cm^{-1}, and $n_{\text{eff}}=3.31$. The samples were cleaved into laser bars, soldered with indium to a copper block, wire bonded, and mounted in a cryostat for the measurements. Typical low-temperature (8 K) laser emission spectra for the two samples are reported in Fig. 2. The lasers oscillate on several longitudinal modes. In both samples, the spacing between them is smaller (~25%) than the one predicted from the computed effective refractive index of the fundamental waveguide mode (1.5 cm^{-1} vs ~2 cm^{-1}), indicating a stronger penetration of the mode into the metallic layer.

Figure 3 reports the light output versus current ($L-I$) characteristic of the lasers at various heat-sink temperatures. The optical power was measured with $f/1$ KBr optics and a LN_2-cooled HgCdTe detector calibrated using a Golay cell detector.

At liquid-helium temperatures the threshold current densities are $J_{\text{th}}=4.1$ and 4.6 kA/cm^2, respectively, for samples D2691 ($\lambda=21.5$ μm) and D2696 ($\lambda=24$ μm). We can calculate the threshold current density for QC lasers:[14]

$$J_{\text{th}}=\frac{1}{\tau_{II}(1-\tau_I/\tau_{II,I})}\,\frac{\epsilon_0\lambda n_{\text{eff}}L_p 2\gamma}{4\pi q\Gamma z^2}(\alpha_m+\alpha_w), \tag{1}$$

where ϵ_0 is the vacuum permittivity constant, n_{eff} is the effective refractive index of the waveguide, L_p is the length of one stage, 2γ is the full width at half maximum of the electroluminescence, q the electron charge, Γ the optical confinement factor, α_m the mirror losses, and α_w the waveguide losses. Since it was not possible to detect the electroluminescence as a result of the low power and the less-sensitive detectors, we employed an estimate $2\gamma=5$ meV for the width of the gain spectrum. This is the value obtained for a $\lambda=19$ μm QC laser.[15] It represents an upper limit since the electroluminescence width typically decreases with increasing wavelength.

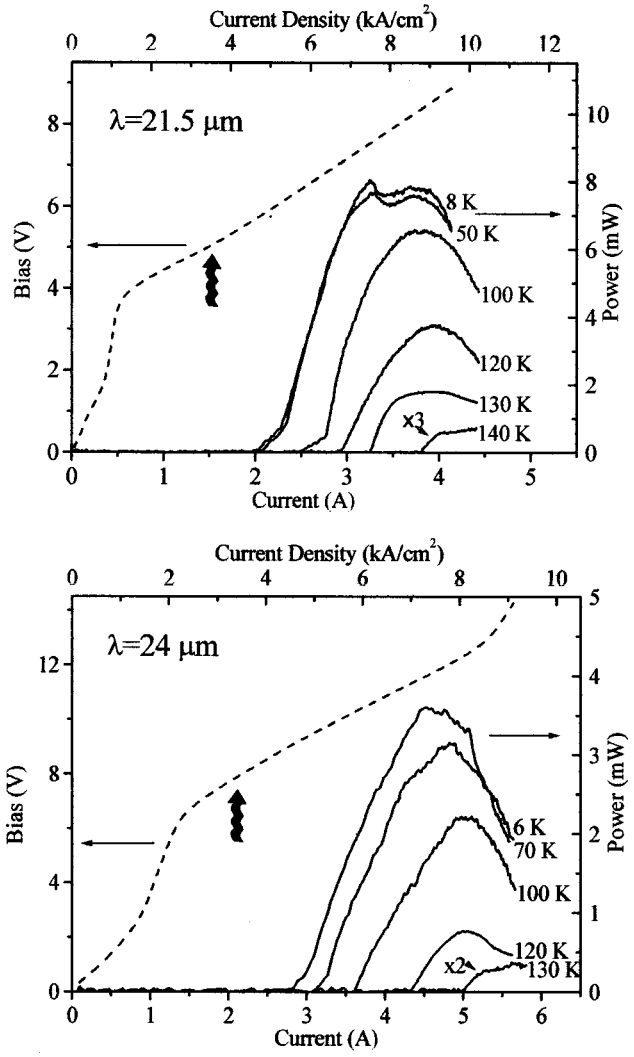

FIG. 3. $L-I$ characteristics of the $\lambda=21.5$ μm and $\lambda=24$ μm lasers for a 1.5-mm-long, 31-μm, and 36-μm-wide device, respectively, operated in pulse mode (50 ns pulse width, 5 kHz repetition rate) at various heat-sink temperatures and using a liquid-nitrogen-cooled HgCdTe detector. The dashed line is a current–voltage ($I-V$) curve at 8 K for the same devices. The wavy arrows indicate the theoretical turn-on voltages (i.e., electric field times the total length of active regions and injectors).

We calculate $J_{th}=1.15$ kA/cm^2 and $J_{th}=1$ kA/cm^2 for samples D2691 and D2696, respectively. The considerable discrepancy with the experimental values originates from various factors; in particular, the overestimate of the nonradiative relaxation times and the underestimate of the waveguide losses. The former is due to the presence of the two-phonon resonances, not included in our model used to calculate nonradiative scattering times. The greater optical loss is related to the deeper than expected penetration of the waveguide mode into the metallic layer, as also revealed by the considerable larger effective refractive index—extracted from the Fabry–Pérot spectrum—with respect to the predicted one. Additionally, even if the turn-on voltages of the lasers are in very good agreement with the calculated ones, the voltage versus current characteristics (see Fig. 3) at low currents indicate that there is tunneling between miniband I of consecutive stages, a process that can induce nonunity carrier injection.

While the surface-plasmon waveguide solution provides very high performance for long-wavelength $\lambda=17-24$ μm QC lasers, it is obvious from the calculations that in the quest for the realization of a QC laser at wavelengths on the lower-energy side of the reststrahlen band ($\lambda>50$ μm), the waveguide design must be further improved. For these reasons, we designed and fabricated a laser based on the same active region as sample D2691 ($\lambda=21.5$ μm), in which the low-doped ($n\sim7\times10^{16}$ cm^{-3}) InGaAs layer below the cascade stack is replaced by a 750-nm-thick highly doped n^{++}-InGaAs layer. The n^{++}-doped semiconductor acts as a bottom ''metal,'' thus realizing a double-sided surface-plasmon waveguide, with an extremely high calculated confinement factor $\Gamma\sim0.98$. However, in order to keep the calculated waveguide losses at the same level of sample D2691, we doubled the number of the active region and injectors. The device exhibited a threshold current density of $J_{th}=7.1$ kA/cm^2, approximately 1.7 times the threshold of the single-sided surface-plasmon sample D2691. The discrepancy between the computed and measured longitudinal mode spacing is larger, indicating a stronger penetration of the mode into the n^{++} layer, the doping of which cannot be increased indefinitely. However, the result is encouraging since the waveguide loss of a double-surface-plasmon waveguide can only decrease when we move from 21.5/24 μm to longer wavelengths below the reststrahlen band ($\lambda>50$ μm). This is also the first working double-plasmon laser, which provides the proof of principle for the suggested waveguide configuration for any far-submillimiter-wavelength QC laser.

This material is based upon work supported in part by DARPA/ARO under Contract No. DAAD19-00-C-0096.

[1] C. Gmachl, F. Capasso, R. Köhler, A. Tredicucci, A. L. Hutchinson, D. L. Sivco, J. N. Baillargeon, and A. Y. Cho, IEEE Circuits Devices Mag. **16**, 10 (2000).
[2] R. Paiella, F. Capasso, C. Gmachl, C. G. Bethea, D. L. Sivco, J. N. Baillargeon, A. L. Hutchinson, A. Y. Cho, and H. C. Liu, IEEE Photonics Technol. Lett. **12**, 780 (2000).
[3] R. Paiella, F. Capasso, C. Gmachl, D. L. Sivco, J. N. Baillargeon, A. L. Hutchinson, A. Y. Cho, and H. C. Liu, Science **290**, 1739 (2000).
[4] C. Sirtori, P. Kruck, S. Barbieri, P. Collot, J. Nagle, M. Beck, J. Faist, and U. Oesterle, Appl. Phys. Lett. **73**, 3486 (1988).
[5] C. Gmachl, H. M. Ng, and A. Y. Cho, Appl. Phys. Lett. **77**, 334 (2000).
[6] M. Rochat, J. Faist, M. Beck, U. Oesterle, and Marc Ilegems, Appl. Phys. Lett. **73**, 3724 (1998).
[7] E. S. Koteles and W. R. Datars, Can. J. Phys. **54**, 1676 (1974); Solid State Commun. **19**, 221 (1976).
[8] A. Tredicucci, C. Gmachl, F. Capasso, D. L. Sivco, A. L. Hutchinson, and A. Y. Cho, Appl. Phys. Lett. **76**, 2164 (2000), and references therein.
[9] A. Tredicucci, F. Capasso, C. Gmachl, D. L. Sivco, A. L. Hutchinson, and A. Y. Cho, Appl. Phys. Lett. **73**, 2101 (1998).
[10] C. Sirtori, F. Capasso, J. Faist, and S. Scandolo, Phys. Rev. B **50**, 8663 (1994).
[11] R. Colombelli, F. Capasso, C. Gmachl, A. Tredicucci, A. M. Sergent, A. L. Hutchinson, D. L. Sivco, and A. Y. Cho, Appl. Phys. Lett. **77**, 3893 (2000), and references therein.
[12] Nonradiative scattering times are calculated considering LO phonon emission only.
[13] C. Sirtori, C. Gmachl, F. Capasso, J. Faist, D. L. Sivco, A. L. Hutchinson, and A. Y. Cho, Opt. Lett. **23**, 1366 (1998).
[14] A. Tredicucci, F. Capasso, C. Gmachl, D. L. Sivco, A. L. Hutchinson, and A. Y. Cho, Appl. Phys. Lett. **73**, 2101 (1998).
[15] A. Tredicucci, C. Gmachl, M. W. Wanke, F. Capasso, A. L. Hutchinson, D. L. Sivco, S. G. Chu, and A. Y. Cho, Appl. Phys. Lett. **77**, 2286 (2000).